Supplementary Information (SI) for Lab on a Chip.

Supplementary Information

Systematic characterization and mechanistic insights into ultrasonically actuated sharp-tip capillary droplet generation

Qi Zhang[1], *Li Ran*[1], *and Gang Li*[1, *]

[1]*Key Laboratory of Optoelectronic Technology and Systems, Ministry of Education, Defense Key Disciplines Lab of Novel Micro-Nano Devices and System Technology, Chongqing University, Chongqing 400044, China*

*Email address: gang_li@cqu.edu.cn (G. Li)

S1. Derivation of the equivalent centrifugal force acting on a liquid element at the ultrasonically vibrated capillary tip

The ultrasonically vibrated capillary can be regarded as a cantilever beam system (fixed at one end, free at the other), and its displacement field under flexural vibration can be described using Euler-Bernoulli beam theory. The vibration mode depends on the driving frequency: if the driving frequency approaches the capillary's natural frequency, it may excite either the fundamental bending mode (first-order mode) or higher-order modes.

In a non-inertial reference frame, the equivalent centrifugal force acting on a liquid element at the capillary tip is given by:

$$F_{\mathrm{c}} = \frac{dm \cdot v^2}{r} \qquad \text{(S1)}$$

where dm is the infinitesimal liquid mass element, v is the tangential speed of the element (along its trajectory), and r is the instantaneous radius of curvature of the trajectory.

Assuming the displacement of the capillary tip follows $y(t)=A\sin(\omega t)$, where A is the amplitude (determined by the piezoelectric driving voltage and capillary stiffness), and $\omega=2\pi f$ (f: driving frequency). The tangential velocity is:

$$v(t) = \frac{dy}{dt} = A \cdot \omega \cdot \cos(\omega t) \qquad \text{(S2)}$$

The radius of curvature r depends on the capillary's flexural deformation and is governed by its vibration mode. In this context, we may approximate r as the distance from the capillary's free end to the nearest node of the standing wave, giving:

$$r \approx \frac{L}{2n-1} \tag{S3}$$

here, L is the distance from the PZT to the capillary free end, n denotes the mode order. Combining Equations (S1), (S2), and (S3) yields:

$$F_{\mathrm{c}} = (2n-1)\frac{dm \cdot A^2 \cdot \omega^2 \cdot \cos^2(\omega t)}{L} \tag{S4}$$

Section S2. Scaling analysis of both opposing η_c-dependent effects

This section provides an order-of-magnitude comparison between the two competing η_c-dependent mechanisms highlighted in the revised manuscript—**(A) amplitude damping** and **(B) neck-thinning delay**—to rationalize why the generated droplet volume V_{drop} exhibits only a weak net dependence (slightly increase) with increasing continuous-phase viscosity η_c. The estimates below are intended for **scaling comparison only** and do not rely on any parameter fitting; they merely illustrate that the two effects can be comparable in magnitude over the experimentally explored viscosity range.

S2.1 Scaling form for droplet volume during the active window

The generated droplet volume is determined by the time integral of the outflow rate during the active actuation window t_{active} (Equation (8) in the manuscript):

$$V_{\mathrm{drop}} = \int_0^{t_{\mathrm{active}}} Q_{\mathrm{out}}(t)\, dt.$$

The outflow rate through the emitted thread/neck can be approximated by a hydraulic-conductance form (Equation (9) in the manuscript):

$$Q_{\mathrm{out}}(t) \propto \frac{r_i(t)^4}{8\eta_d\, l(t)}\left(p_c(t) - p_n(t)\right),$$

where $r_i(t)$ is the instantaneous neck radius, $l(t)$ is the characteristic hydraulic length, and η_d is the dispersed-phase viscosity. This expression emphasizes the strong geometric sensitivity of the outflow through the fourth-power dependence on r_i.

To compare viscosity-dependent contributions, it is convenient to express the droplet volume in the following multiplicative scaling form:

$$V_{\mathrm{drop}} \propto \int_0^{t_{\mathrm{active}}} \underbrace{\Delta p(t)}_{\text{pumping strength}} \quad \underbrace{\frac{r_i(t)^4}{\eta_d\, l(t)}}_{\text{hydraulic conductance}} \quad dt, \qquad \Delta p(t) \equiv p_c(t) - p_n(t).$$

In our model, the pumping strength scales with the actuation amplitude as $\Delta p \propto F_c \propto A^2$. Therefore, changes in η_c may influence V_{drop} through (i) changes in A (amplitude damping) and/or (ii) changes in $r_i(t)$ within the same t_{active} window (neck-thinning delay).

S2.2 Effect A: amplitude damping reduces pumping strength (tends to decrease V_{drop})

An increased η_c can impose larger hydrodynamic loading on the vibrating capillary tip, decreasing the effective vibration amplitude A. Since the centrifugal pumping force scales as $F_c \propto A^2$, the droplet volume inherits a quadratic dependence on A: $V_{\mathrm{drop}} \propto A^2$ × (geometry-time integral). Accordingly, the leading-order fractional change of droplet volume attributable to amplitude damping scales as

$$\left(\frac{\Delta V}{V}\right)_A \approx 2\,\frac{\Delta A}{A}.$$

A representative scaling estimate is as follows: if the effective amplitude were reduced by $\sim 10\%$ over the explored η_c range, then A^2 would decrease by $(0.9)^2 \approx 0.81$, i.e., an $\sim 19\%$ reduction tendency in the pumping-controlled contribution to V_{drop}.

S2.3 Effect B: delayed neck thinning increases effective conductance (tends to increase V_{drop})

Increasing η_c weakens acoustic streaming, with $U_s \propto 1/\eta_c$. A reduced streaming velocity slows the neck-thinning/elongation dynamics during the active phase. As a result, within the same t_{active} pulse, the neck can remain **relatively thicker (lower hydrodynamic resistance)** for a longer fraction of time, increasing the time-integrated hydraulic conductance and thus increasing V_{drop}.

Because the hydraulic conductance scales as r_i^4, modest changes in the effective neck radius can produce significant changes in Q_{out}:

$$\frac{\Delta Q_{\mathrm{out}}}{Q_{\mathrm{out}}} \sim \frac{\Delta(r_i^4)}{r_i^4}.$$

A representative scaling estimate is: if delayed thinning results in an effective neck radius that is only ~5% larger during a substantial portion of the active window, then the conductance factor increases by

$$\frac{\Delta(r_i^4)}{r_i^4} = (1.05)^4 - 1 \approx 0.22,$$

corresponding to an ~22% increase tendency in the conductance-controlled contribution to V_{drop}.

S2.4 Comparison of magnitudes and implication for weak net η_c dependence

Combining the above, the droplet volume can be viewed as the product of an amplitude-controlled factor and a geometry-controlled factor:

$$V_{\mathrm{drop}} \propto A^2 \int_0^{t_{\mathrm{active}}} \frac{r_i(t)^4}{\eta_d\, l(t)}\, dt.$$

The scaling estimates in Sections S2.2–S2.3 show that a moderate reduction of A (e.g., $\sim 10\%$, yielding an $\sim 19\%$ decrease in A^2) can be offset by a modest reduction in the degree/rate of neck constriction (e.g., $\sim 5\%$ change in effective r_i, yielding an $\sim 22\%$ increase in r_i^4). This comparison illustrates that the two opposing η_c-dependent contributions can be comparable in magnitude, which naturally leads to a **weak net dependence** of V_{drop} on η_c.

Consistent with this interpretation, the experimentally measured dependence in Fig. 3d is weak, with small slopes (0.028, 0.009, and 0.003 for $t_{\mathrm{active}} = 5$, 10, and 25 ms, respectively). The slight increase of droplet volume with η_c indicates that, within our parameter range, the conductance increase caused by delayed neck thinning can marginally dominate over the decrease in pumping strength caused by amplitude damping.

Section S3. Finite element analysis of the coupled PZT–capillary assembly

To identify the resonance frequencies of the coupled assembly, quantify how the tip displacement depends on excitation frequency, and provide a physics-based rationale for selecting the working carrier frequency used in experiments, we conducted a structural finite element analysis (FEA) in COMSOL Multiphysics®.

S3.1 Geometry and components

The simulated assembly consisted of three parts: (1) a circular PZT disk transducer, (2) an epoxy adhesive layer, and (3) a borosilicate glass capillary. The PZT disk had a diameter of 27 mm. The capillary had an outer/inner diameter of 700/500 μm in the straight section and was modeled with a tapered distal end to represent the pulled sharp tip used for droplet generation. In the assembled device, the tip extended beyond the PZT edge by an overhang length of 15 mm; this overhang was used in the model to capture the effective cantilevered section responsible for tip motion. The adhesive was modeled as a uniform elastic layer that bonds the capillary to the PZT at the designed contact region.

S3.2 Material properties and assumptions

The PZT was modeled as a linear piezoelectric material under small-signal harmonic excitation. The glass capillary and epoxy were modeled as linear elastic solids. The analysis focused on the intrinsic structural response of the coupled assembly; unless otherwise stated, fluid loading (added mass and viscous damping from surrounding liquids) was not explicitly included. This assumption is appropriate for identifying resonance locations and relative amplification trends of the structure, which were then used to guide experimental frequency selection.

S3.3 Boundary conditions and excitation

The PZT disk was mechanically constrained at its mounting region to prevent rigid-body motion, representing attachment/support in the experimental configuration. Electrical excitation was applied to the PZT electrodes as a harmonic voltage, and the resulting steady-state displacement field of the coupled structure was solved in the frequency domain. Two displacement metrics were extracted from the simulations:
(i) the displacement amplitude of the PZT (representative point on the PZT surface) and (ii) the displacement amplitude at the capillary tip (defined at the distal end of the tapered tip).

S3.4 Eigenfrequency (modal) analysis

An eigenfrequency analysis was first performed to identify the natural modes of the coupled structure within the range relevant to experiments. Multiple structural modes were found across the kHz–hundreds-of-kHz range. These modes provide the basis for interpreting frequency-response peaks and explain why the tip motion can be strongly amplified when driving near specific resonances of the coupled assembly.

S3.5 Frequency-response analysis and selection of working carrier frequency

A frequency sweep was then performed to obtain the harmonic response spectrum of the assembly. The simulated PZT displacement amplitude shows a prominent low-frequency resonance near 4.6 kHz (Fig. S6a), which corresponds to a resonance of the bare PZT response. In contrast, the simulated tip displacement spectrum exhibits a dominant resonance peak near 100.4 kHz (Fig. S6b), indicating that this coupled-system resonance produces the strongest vibration at the droplet-forming location (the capillary tip). To assess how efficiently vibrational energy can be delivered at different resonances, we further plotted the product of tip displacement amplitude and frequency ($A_{\mathrm{tip}} \times f$) (Fig. S6c). This metric is commonly used as a proxy for actuation strength when both displacement amplitude and oscillation frequency contribute to fluidic forcing in ultrasound-driven systems. The $A_{\mathrm{tip}} \times f$ spectrum also peaks at ~100.4 kHz, supporting the selection of this resonance as the experimental working carrier frequency.

S3.6 Implications for harmonics and stability under sinusoidal carrier actuation

The frequency-response spectra (Fig. S6) show that the coupled structure possesses multiple resonances. However, in experiments the PZT is driven by a single sinusoidal carrier frequency that is tuned to the dominant tip-amplifying resonance. Under this near-resonant single-frequency excitation, the structural response is dominated by the driven resonance and the motion at the tip is repeatable and stable. While additional peaks exist in the spectrum, their contributions are minimal when the drive frequency is held at the selected resonance. Therefore, stable droplet generation is achieved by operating in a mode-dominant regime in which the droplet-forming location (the tip) experiences maximized displacement at the chosen carrier frequency.

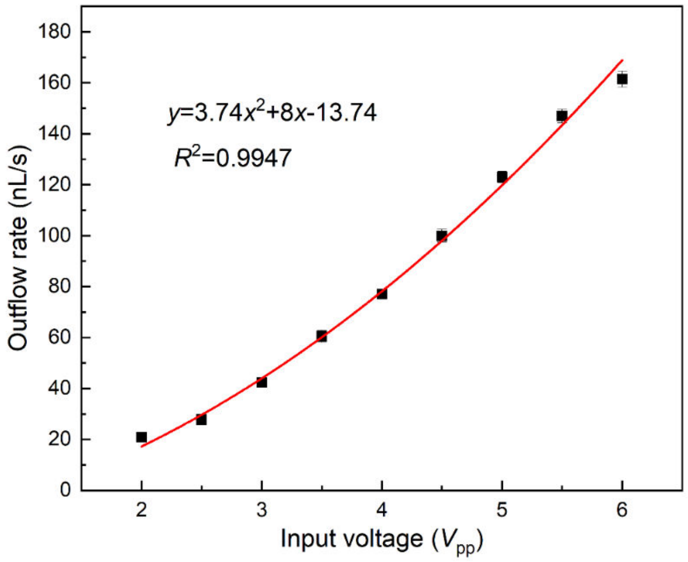

Fig. S1 Experimental measurement of the volumetric outflow rate Q_{out} from the capillary tip under continuous ultrasonic actuation (without AM modulation). The reduction of the liquid column in the feeding tubing was tracked over time to calculate Q_{out}. The quadratic fit confirms $Q_{\mathrm{out}} \propto V_{\mathrm{pp}}^2$, consistent with the theoretical model (Eq. 12).

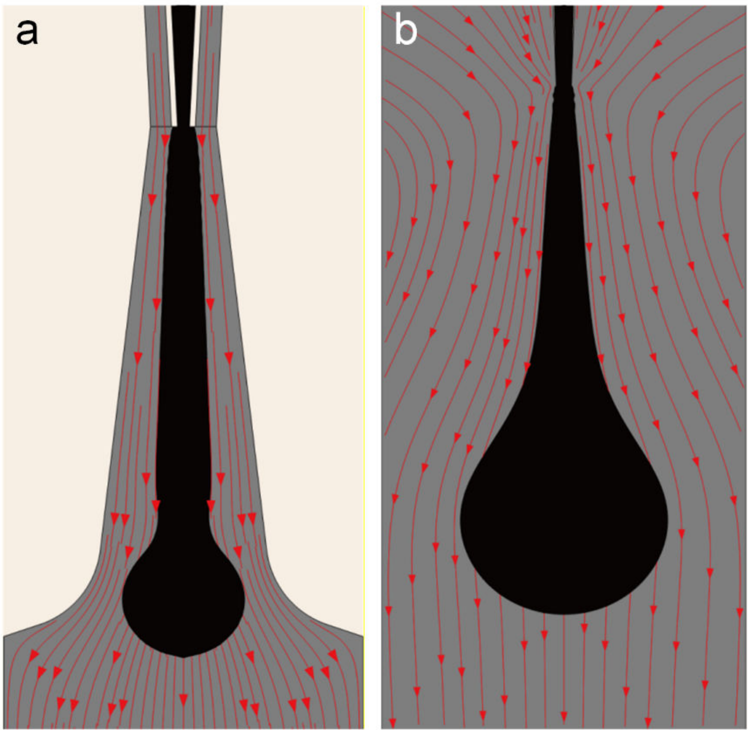

Fig. S2 Comparison of near-tip continuous-phase flow-field distributions illustrating the hydrodynamic equivalence between (a) the streaming-induced squeezing field generated around the oscillating tapered capillary tip (time-averaged vortex-driven co-flow) and (b) the pressure-driven co-flow focusing surrogate model. The velocity/streamline patterns show a highly similar shear/squeezing field acting on both sides of the dispersed-phase filament near the outlet, supporting the use of the co-flow model as a physics-preserving surrogate for interrogating AM-gated necking and pinch-off dynamics.

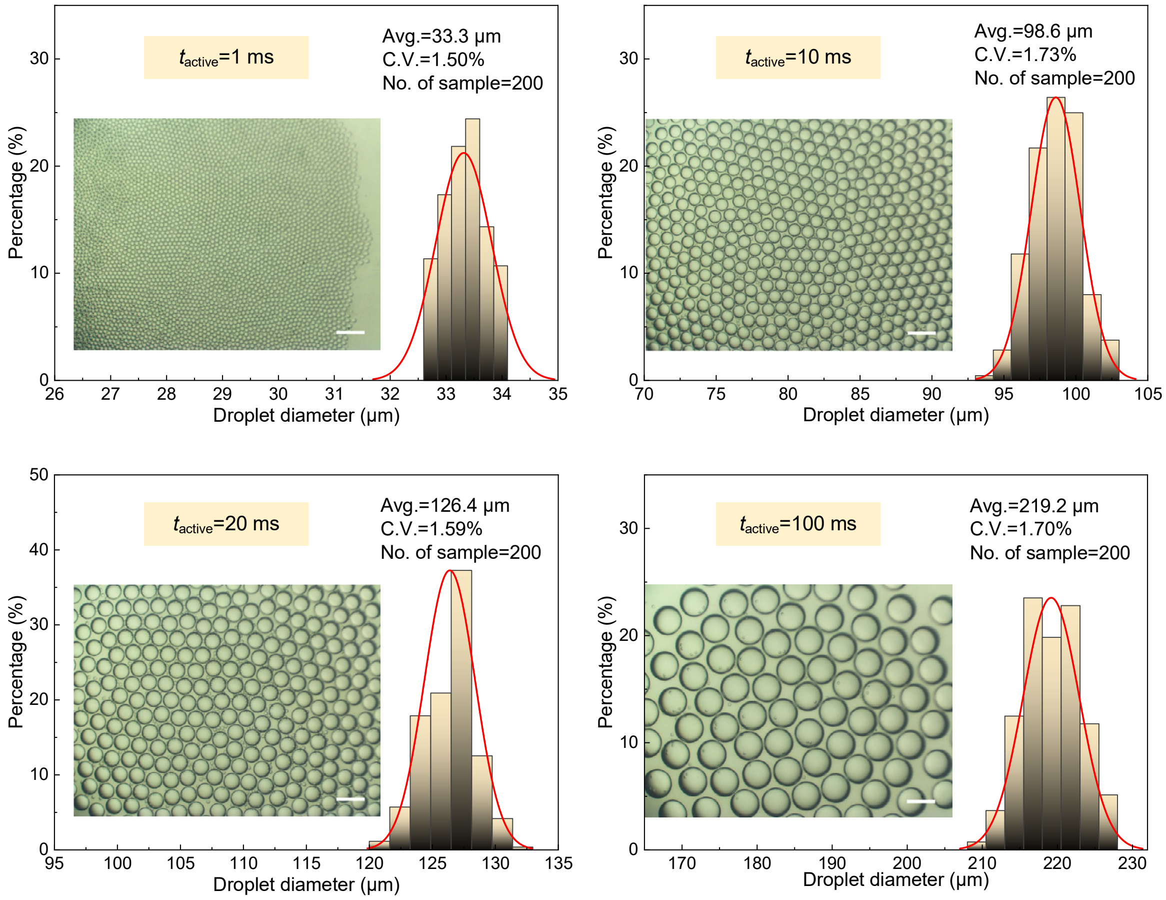

Fig. S3 Monodispersity of droplets across the linear operational regime. Representative statistical analysis of the diameter distribution of droplets generated within the stable AM modulation range (0.25–250 ms). CV values remain below 2%, confirming highly consistent droplet generation within this regime. Scale bar: 200 μm.

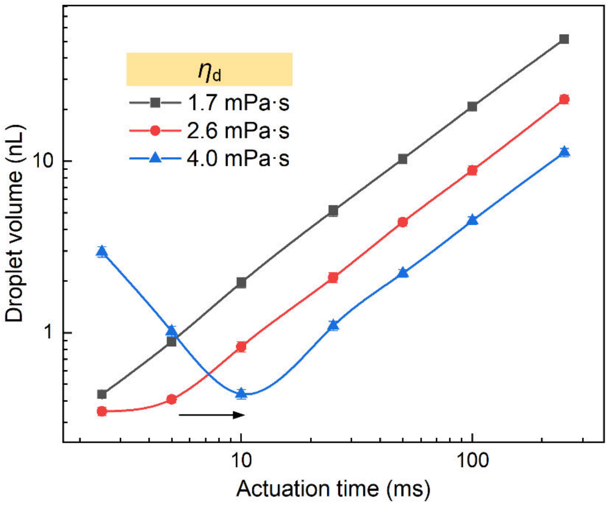

Fig. S4 Hysteresis in droplet volume versus actuation time for dispersed phases with different viscosities. Arrows indicate the direction of actuation time sweep. The minimum volume point (hysteresis point) shifts toward longer driving times with higher viscosity, reflecting delayed pinch-off under viscous dominance.

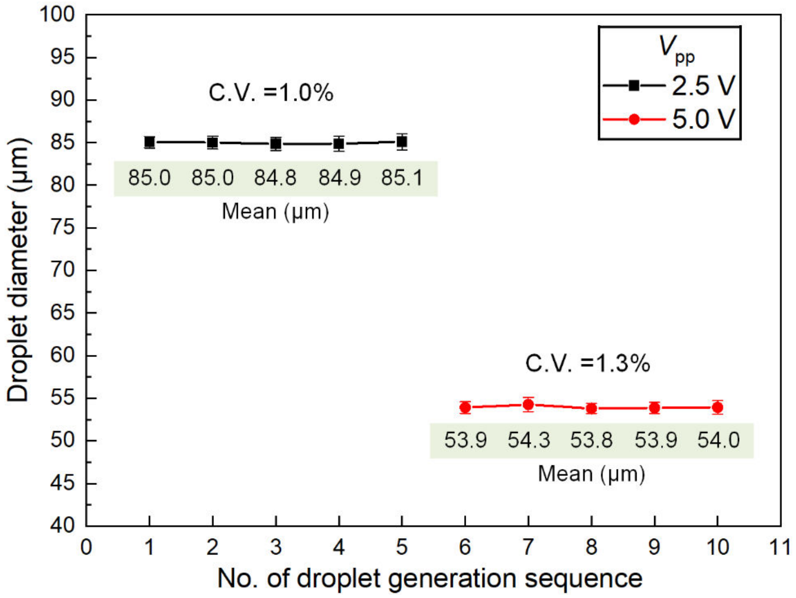

Fig. S5 Inter-run reproducibility of PEGDA microsphere preparation using the ultrasonically actuated sharp-tip capillary platform. Prepared hydrogel microsphere diameter as a function of droplet generation sequence for two independent batches performed at different driving voltages: (top) 2.5 V_{pp} and (bottom) 5 V_{pp}. Each batch comprises five independent runs with turning off acoustic signal, taking out the capillary tip from oil, re-inserting the tip, and restart actuation. Error bars represent standard deviation of droplet diameters within each run. The coefficients of variation (CV) are 1.0% and 1.3% for the 2.5 V_{pp} and 5 V_{pp} batches, respectively, confirming excellent reproducibility across repeated operations.

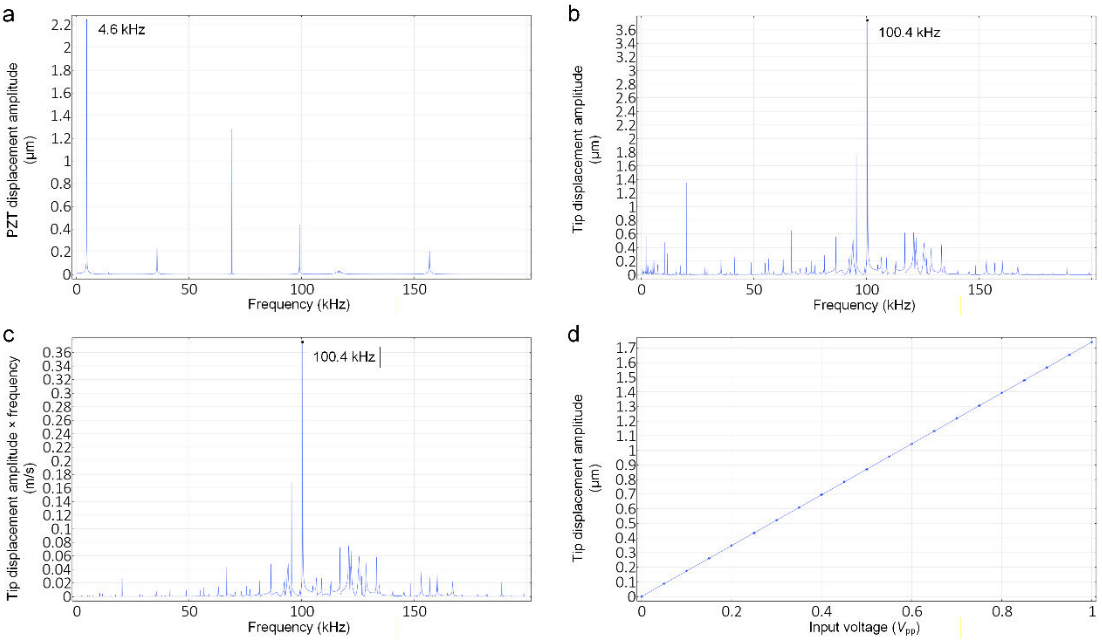

Fig. S6 Frequency-response characterization of the coupled PZT–capillary assembly by structural FEA. (a) Simulated displacement amplitude spectrum of the PZT under harmonic voltage excitation, showing a prominent low-frequency resonance of the transducer near 4.6 kHz. (b) Simulated displacement amplitude spectrum at the capillary tip, showing a dominant tip-amplifying resonance peak near 100.4 kHz for the coupled PZT–capillary assembly. (c) Tip displacement amplitude multiplied by frequency ($A_{\mathrm{tip}} \times f$) as a proxy metric for actuation strength, which also peaks at ~100.4 kHz, supporting the selection of this frequency as the working ultrasonic carrier frequency for droplet generation experiments. (d) Simulated tip displacement amplitude as a function of input voltage V_{pp} at the fixed operating frequency (100.4 kHz), showing an essentially linear relationship ($A_{\mathrm{tip}} \propto V_{\mathrm{pp}}$), consistent with the assumption adopted in the theoretical model (Equation (3)).

Supplementary Videos Legend

Video S1: *Droplet pinch-off process upon cessation of capillary vibration.* Time-lapse microscopy showing Laplace pressure-driven neck thinning and droplet detachment following vibration termination.

Video S2: *Periodic droplet generation under square-wave amplitude modulation (AM).* Droplets are generated synchronously with the modulation signal.

Video S3: *Numerical simulation of droplet formation under AM-modulated flow conditions.* COMSOL Multiphysics simulation of co-flow capillary focusing under periodic inflow conditions. Drive period: 100 ms.

Video S4: *Droplet generation frequency sweep from 2 Hz to 1 kHz.* Demonstration of droplet size and generation rate modulation *via* AM frequency adjustment at a fixed voltage of 8 V.

Video S5: *Droplet formation under very short actuation time.* Illustration of incomplete volumetric displacement and inconsistent droplet size due to system response lag.

Video S6: *Uncontrolled droplet breakup under extended actuation time.* Rayleigh–Plateau instability causes premature thread breakup before vibration cessation.

Video S7: *Failure of droplet ejection under low driving voltage.* Insufficient centrifugal force to overcome interfacial tension prevents dispersed phase pumping.

Video S8: *Jet instability and satellite droplet formation under high voltage.* High Reynolds number flow leads to whipping and irregular droplet emission.

Video S9: *Effect of dispersed phase viscosity on jet stability.* Droplet generation using 1 wt% sodium alginate ($\eta_d \approx 12.7$ mPa·s). Higher viscosity improves jet stability and extends the upper limit of t_{active} to 500 ms.

Video S10: *Programmed generation of dual-volume droplet sequences.* Alternating two different droplet sizes produced using asymmetric AM waveforms with pulse widths of 125 ms and 250 ms.

Video S11: *Programmed generation of triple-volume droplet sequences.* Alternating three droplet sizes produced using asymmetric AM waveforms with pulse widths of 60 ms, 120 ms, and 240 ms.